Supplementary Information for

Tunable, multifunctional opto-electrical response in multilayer $FePS_3$/single-layer MoS_2 van der Waals p-n heterojunctions

*Maria Ramos[1,2]#, Marcos Gadea[1,2]#, Samuel Mañas-Valero[3], Carla Boix-Constant[3], Eudomar Henríquez-Guerra[1,2], María A. Díaz-García[1,2], Eugenio Coronado[3], M. Reyes Calvo[1,2]**

# equal contribution

E-mail: reyes.calvo@ua.es

[1] Departamento de Física Aplicada, Universidad de Alicante, Alicante 03080, Spain

[2] Instituto Universitario de Materiales de Alicante (IUMA), Universidad de Alicante, Alicante 03080, Spain

[3] Instituto de Ciencia Molecular (ICMol), Universitat de València, Paterna 46980, Spain

List of contents

S1. Thickness characterization of $FePS_3$ flakes

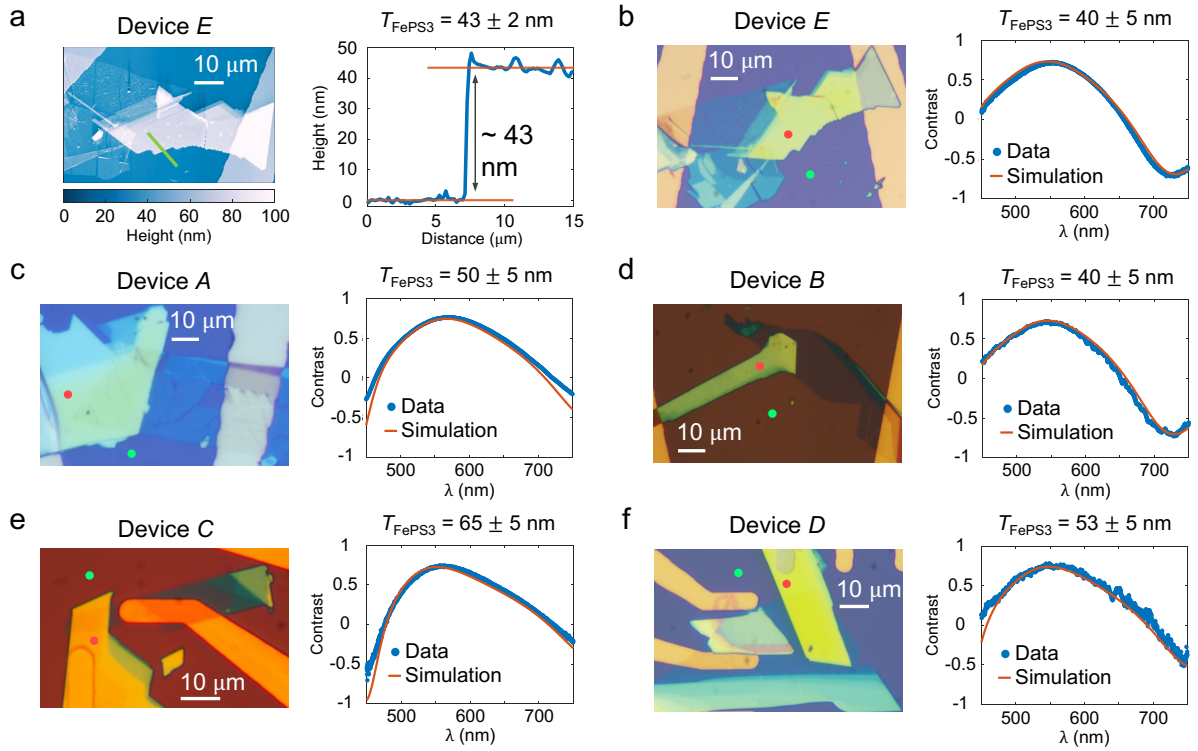

Figure S1. Thickness analysis of the $FePS_3$ flakes in the different heterostructure devices characterized in this work. (a) Left: AFM topographic image of the device shown in (b). Right: Height profile corresponding to the green line marked in the AFM image. (b) Left: Optical microscopy image of a $FePS_3$/1L-MoS_2 junction (device *E*). Right: Optical contrast obtained from micro-reflectance spectroscopy measurements performed on the $FePS_3$ flake on SiO_2/Si (red spot) and the bare SiO_2/Si substrate (green spot). Experimental data is represented by blue dots. The red continuous line represents a simulation of the optical contrast for the multilayer system assuming a SiO_2 thickness of 280 nm and a thickness of 40 nm for the $FePS_3$ flake. Panels (c)-(f) display images of different devices used in this work accompanied by the corresponding experimental optical contrast (blue dots) obtained from the micro-reflectance spectra measured at the spots at $FePS_3$ and substrate marked in the images. The thickness of $FePS_3$ is obtained from the simulation of the optical contrast for the corresponding multilayer system.

The thickness of $FePS_3$ flakes forming the heterostructure devices was determined by micro-reflectance spectroscopy measurements following the methods described in ref. [s1]. Micro-reflectance spectra were collected from a spot diameter of approx. 3 μm, both at locations on the $FePS_3$ flake and at the bare SiO_2/Si substrate (indicated in Fig. S1). The reflectance for the $FePS_3$/SiO_2/Si (R_{FePS3}) and for the SiO_2/Si substrate (R_{SiO2}) can be estimated from a simple model for light propagation in an optical multilayer system (see for instance refs. [s1] and [s2]). The optical contrast can be calculated as $C = (R_{FePS3} - R_{SiO2})/(R_{FePS3} + R_{SiO2})$ and strongly depends on the thickness and refractive index values of the different layers constituting the system. Refractive index values for Si and SiO_2 are taken from Palik *et al.* [s3]. The thickness of the SiO_2 layer is approx. 280 nm. In previous works [s1], we extracted an estimation for the refractive index of $FePS_3$ ($n \sim 2.70$, $k \sim 0.15$, being n and k the real and imaginary parts of the refractive index, respectively) from the analysis of transmittance and optical contrast of samples for which the thickness was precisely identified by AFM measurements. Using these values, we can extract the thickness of the $FePS_3$ flakes by

comparing the experimental data to the results of the contrast simulations. Figure S1 shows the micro-reflectance characterization of $FePS_3$ in different devices used in this work. In Figure S1a-b, we show a comparison of AFM topography and micro-reflectance characterization for the same $FePS_3$ flake, showing a good agreement within error range.

S2. Carrier density and charge transfer in $FePS_3$/1L-MoS_2 heterostructures

Charge transfer estimate from a mass action law model

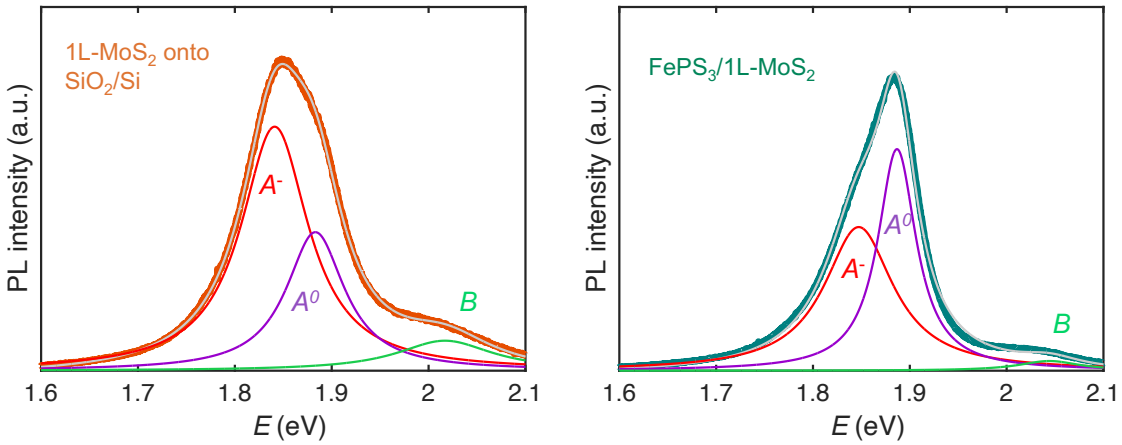

Figure S2. Left: Photoluminescence spectrum taken on device *A* on 1L-MoS_2 on SiO_2 (at the position marked by the red dot in Fig. 1b in the main text). Right: Photoluminescence spectrum taken on device *A* on 1L-MoS_2 below $FePS_3$ flake, at the corresponding green dot in Fig 1b. PL data is fit to the sum of three lorentzian peaks, which are shown in each panel.

The PL signal of the single-layer MoS_2 can be decomposed into three excitonic Lorentzian peaks both for the isolated MoS_2 on SiO_2 and for the heterojunction formed by $FePS_3$/1L-MoS_2. Following previous works [s4], these three peaks can be identified as: X^- peak (trion or negatively charged exciton), the X^0 peak (neutral exciton) and the B peak (neutral exciton). Excitons A and B come from the spin-orbit splitting at the valence band of single-layer MoS_2.

The Lorentzian fits in the figure above show that the main contribution to the PL emission in the 1L-MoS_2 onto SiO_2/Si (left) comes from the negatively charged exciton (X^-), showing the n-type of doping, typical of MoS_2. For the case of the heterojunction, we can observe a change in the spectral weight of the negatively charged exciton (X^-) and the neutral exciton (X^0) compared to the isolated MoS_2. This observation suggests a charge transfer of electrons from the monolayer to the $FePS_3$ flake when both materials are in contact, as described in Refs. [s5, s6]. In a trial to quantify this, we consider the equilibrium between the relative populations of charged and neutral excitonic species, as well as free electrons:

$$X^0 + e \leftrightarrow X^- \qquad \text{(S1)}$$

The equilibrium situation is described by a mass action law, where the population of the 3 species is governed by this rate equation:

$$\frac{N_{X^-}}{N_{X^0}} = K_T \cdot n_{el} \qquad \text{(S2)}$$

where N_{X^-} and N_{X0} are the number of trions and neutral excitons, K_T is the rate constant for trions and n_{el} is the free electron density.

The ratio of the areas under the PL curve for these two contributions, A^- for charged excitons and A^0 for neutral excitons (see Figure S2), is expected to be proportional to the ratio of the respective populations:

$$\frac{A^-}{A^0} \propto \frac{N_{X^-}}{N_{X^0}} \qquad \text{(S3)}$$

Taking this into consideration for the 1L-MoS_2 onto SiO_2/Si and for the heterojunction, a first estimation of the relative change of electron concentration in the monolayer MoS_2, (n_{el}^{con} - n_{el}^{het})/n_{el}^{con}, due to charge transfer when it is placed in contact with $FePS_3$, results in a 43% for the case of device A. Moreover, our previous experimental results on similar heterostructures - except that the single-layer MoS_2 was placed on top of $FePS_3$ - demonstrate a strong tunability of this charge transfer as a function of the $FePS_3$ thickness (see Ref. s6, Figure 2d). In our current work, where the monolayer MoS_2 is underneath a 40-to-60-nm thick $FePS_3$, we observe a similar effect on the PL emission (a reduction in the n-doping of the 1L-MoS_2 upon contact with $FePS_3$), even though if the monolayer material is in contact with the SiO_2 dielectric and part of the light is absorbed by $FePS_3$, preventing an exact comparison between the two sample geometries.

Mobilities and carrier densities for 1L-MoS_2 and 30-nm thick $FePS_3$

An estimate for mobilities and carrier densities of $FePS_3$ and 1L-MoS_2 has been obtained from two-terminal electrical measurements as a function of the applied gate voltage in field-effect transistor devices. The mobilities are calculated as $\mu = \frac{L}{WC}\frac{\partial G}{\partial V_g}$, being L and W the channel's length and width, respectively, C is the oxide capacitance per unit area $C = \varepsilon_0\varepsilon_r/d$, where ε_0 and ε_r are the vacuum and relative permittivities, and d the capacitor thickness. G is the conductance and V_g is the applied gate voltage.

The mobility of $FePS_3$ has been calculated from the conductance values as a function of applied gate voltage for a 30-nm thick flake, using data from Ramos et al. (ref. s1). Around zero-gate, we obtain $\mu_{FePS3} = 9\cdot10^{-3}$ $cm^2V^{-1}s^{-1}$. Similarly, the mobility of 1L-MoS_2 has been obtained from the conductance as a function of gate voltage from data presented in Figure S3, being $\mu_{MoS2} = 3.5\cdot10^{-2}$ $cm^2V^{-1}s^{-1}$, which is similar to other values reported in the bibliography (see for instance Radisavljevic et al. *Nat. Nanotech.*, 6, 2011, ref. s7).

Carrier densities can be subsequently extracted through the relations between conductivity (σ), conductance (G) and mobility (μ): $\sigma = G\frac{L}{Wt}$ and $\sigma = n\mu e$. Thus, the carrier density is given by: $n = G\frac{L}{Wt\mu e}$, where L, W, t and e are the length and width of the channel, the material's thickness and the electron charge, respectively.

Based on the previous expression, we obtain a carrier density of $n_{FePS3} = 5.4\cdot10^{17}$ cm^{-3} for $FePS_3$, and $n_{MoS2}= 4.4\cdot10^{19}cm^{-3}$ for MoS_2. Taking into account the one-layer thickness of the MoS_2 (t_{MoS2} = 0.78 nm), we obtain n_{2D} (MoS_2) = n_{3D}*t = $3\cdot10^{12}$ cm^{-2} for a single-layer MoS_2. This result is in good agreement with the density of carriers reported for single-layer MoS_2 in other works (see Radisavljevic et al. *Nat. Mater.*, 12, 2013, ref. s8).

From these calculations we find that the carrier density of $FePS_3$ is almost two orders of magnitude lower than that of 1L-MoS_2. This is consistent with our previous observations in ref. s6, where the charge transferred between the two materials upon contact is limited by the available carriers at the $FePS_3$ flake (lower carrier density material), growing with increasing $FePS_3$ thickness.

Table S1. Calculated mobilities and carrier densities for 30-nm thick $FePS_3$ and single-layer MoS_2.

	$FePS_3$	**1L-MoS_2**
Mobility	$9 \cdot 10^{-3}$ $cm^2V^{-1}s^{-1}$	$3.5 \cdot 10^{-2}$ $cm^2V^{-1}s^{-1}$
Carrier density	$5.4 \cdot 10^{17}$ cm^{-3}	$n_{3D} = 4.4 \cdot 10^{19}$ cm^{-3} $n_{2D} = 3 \cdot 10^{12}$ cm^{-2}

Carrier density estimation for MoS_2 in the heterostructure

If we recall the mass action law employed to estimate the amount of charge transferred in our devices, taking into account that the ratio of the trion spectral weights between the heterostructure and the control samples must be equal to the ratio of the carrier densities between the heterostructure and the control samples, then we can estimate the carrier density of the heterostructure (device *A*) as:

$$(A^-/A^0)^{het}/(A^-/A^0)^{con} = n_{el}^{het}/n_{el}^{con} = 0.57. \quad (S4)$$

Thus, $n_{el}^{het} = 0.57 n_{el}^{con}$. If we assume the previously calculated carrier density for MoS_2 ($n_{3D} = 4.4 \cdot 10^{19}$ cm^{-3}), then the carrier density for the heterostructure is $2.5 \cdot 10^{19}$ cm^{-3}. The reduced carrier density in the heterostructure, compared to the single-layer MoS_2 directly placed onto SiO_2, points to a reduced n-doping of MoS_2 when interfaced with $FePS_3$.

Depletion region picture

To estimate the length of the depletion region in the heterostructure, we assume the system to be an abrupt p-n junction at equilibrium, to which no bias voltage is applied, and that both MoS_2 (n-side) and $FePS_3$ (p-side) host shallow dopants and therefore the density of acceptors and donors can be approximated by the density of free carriers, that is, $N_A \sim n_h$ in $FePS_3$ and $N_D \sim n_e$ in MoS_2.

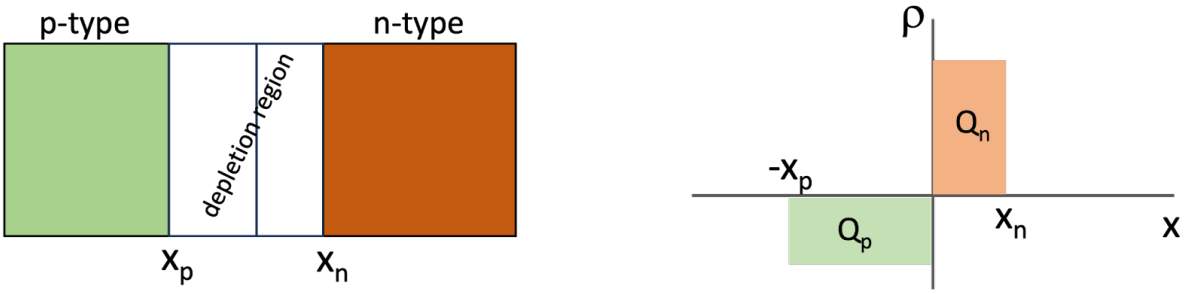

Sketch. Left: Sketch for an abrupt pn-junction where the x_p and x_n depletion regions are marked. Within those limits, charge is proportional to the density of acceptors and donors respectively at the p and n sides. Right: Charge density as a function of position across the junction. The blue and red areas represent the total charge at the p and n region respectively.

After bringing the two materials into contact, once equilibrium is reached, charge neutrality implies that the total charge on the p-side of the depletion region $Q_p = qx_pN_A \sim qx_pn_h$ must be equal to the charge on the n-side $Q_n = qx_nN_D \sim qx_pn_e$. From this equality $Q_p = Q_n$, a the depletion region length on both sides of the junction (x_{MoS2} and x_{FePS3} respectively) can be expressed as a function of the carrier densities of each side far from the junction: $x_{MoS2}/x_{FePS3} \sim n_{FePS3}/n_{MoS2} \sim 100$, according to the values for carrier densities calculated in this section.

We interpret this result as follows. To fully deplete a single layer of MoS_2, for which x_n is limited by its thickness (~ 0.7 nm), a depletion region of length ~ 70 nm would be generated on the $FePS_3$ side. If we bring $FePS_3$ flakes thinner than 70 nm into contact with 1L-MoS_2, full depletion cannot be achieved and the resulting density of carriers in MoS_2 will depend on the thickness of $FePS_3$. Assuming that $FePS_3$ flakes are fully depleted, charge neutrality implies that $t_{FePS3}*n_{FePS3}=t_{1L\text{-}MoS2}*n_{MoS2}$. As long as t_{FePS3} is below 70 nm, $n_{MoS2} = t_{FePS3}*n_{FePS3}/t_{1L\text{-}MoS2}$. For example, in a junction with a $FePS_3$ flake of 35 nm, the carrier density of MoS_2 would be expected to be reduced to a half. This is in a good qualitative agreement to our estimation of charge transfer from mass action law predicts a change from $4.4 \cdot 10^{19}$ to $2.5 \cdot 10^{19}$ 1/cm^3 in the carrier density of single-layer MoS_2 after charge transfer in contact with a 40-nm thick $FePS_3$ flake.

S3. 1L-MoS_2 FET *I-V* characteristics as a function of back-gate voltage

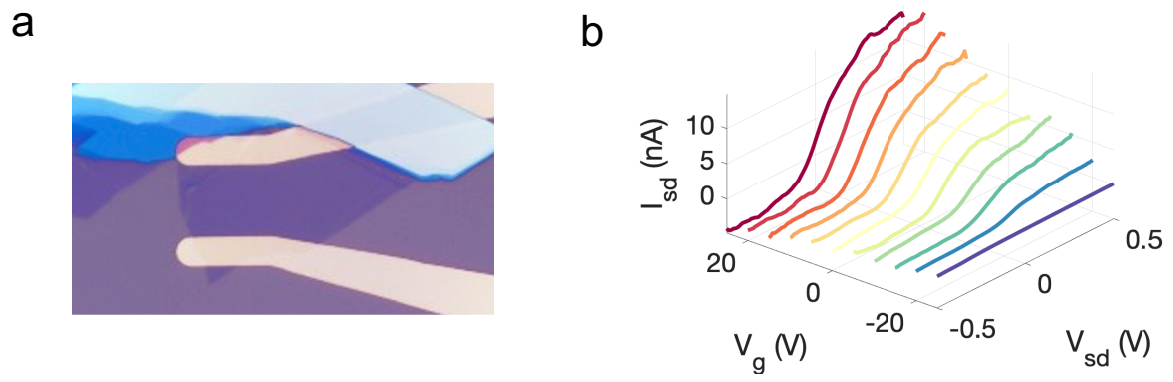

Figure S3. (a) Optical image of a single-layer MoS_2 field effect transistor (FET) device. The distance between the gold leads is 20 μm. (b) Source-drain current-voltage characteristics for a 1L-MoS_2 FET device as a function of back-gate voltage (V_g).

S4. Rectification ratio determination for a $FePS_3$/1L-MoS_2 diode (device *A*) and comparison with other van der Waals heterojunctions

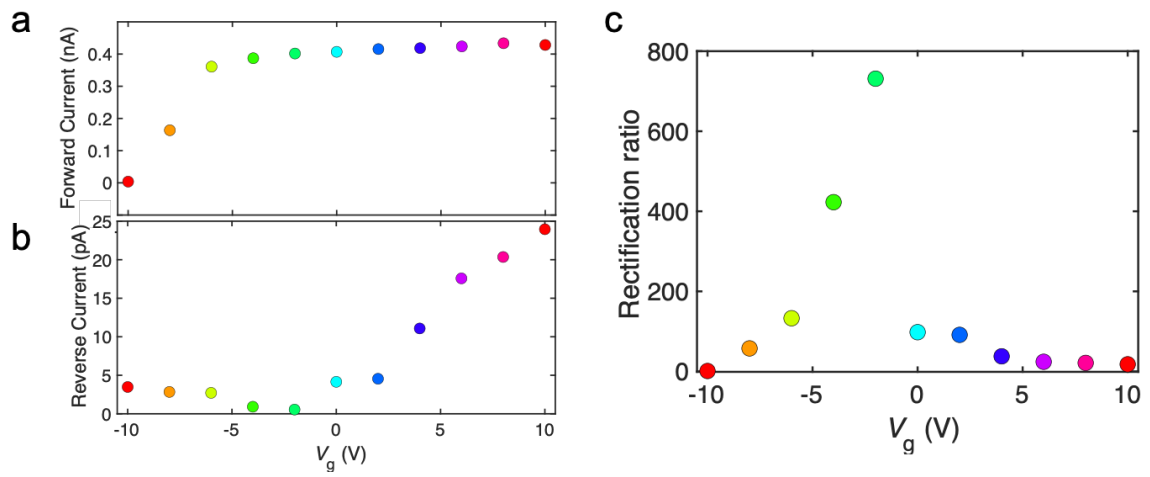

Figure S4. (a) Forward current at V_{sd} = 0.5 V as a function of gate voltage (V_g). (b) Reverse current at V_{sd} = -0.5 V as a function of gate voltage (V_g). (c) Rectification ratio as a function of the applied gate voltage V_g for device *A,* obtained from the $I_{sd} - V_{sd}$ curve shown in Fig. 1g at V_{sd} = 0.5 V.

The rectification ratio is obtained as the quotient between the currents measured for a certain value of V_{sd} with opposite polarities. A maximum rectification ratio of RR ~ 750 is obtained for device *A* at V_g = -2 V and for $|V_{sd}|$ = 0.5 V.

Below, a comparative table including rectification ratios in van der Waals heterojunctions containing MoS_2 is included.

Table S2. Rectification ratios of different van der Waals heterojunctions containing MoS_2. *1L* indicates single layer.

Layer structure	Rectification ratio	V_{sd} (V)	V_g (V)	Reference
Black P/1L-MoS_2	10^5	2	-30	[s9]
Black P/MoS_2	182	1	10	[s10]
Franckeite/MoS_2	400	0.75	40	[s11]
p-MoS_2/n-MoS_2	250	1	0	[s12]
$ReSe_2$/MoS_2	500	5	0	[s13]
$FePS_3$/1L-MoS_2	**750**	**0.5**	**-2**	**This work**

S5. Ideality factor for $FePS_3$/1L-MoS_2 photodiodes

In the Shockley model, the ideality factor, n_{id}, is an experimental parameter that shows the deviation of the measured I_{sd}-V_{sd} curve from an ideal diode, due to second-order effects occurring in the system [s10, s11]. The diode equation in this model has the following expression:

$$I_{\mathrm{sd}} = I_0 \left(\exp\left(\frac{\mathrm{e}V_{\mathrm{sd}}}{n_{\mathrm{id}} \mathrm{k_B} T} \right) - 1 \right) - I_{\mathrm{ph}} \qquad \text{(S5)}$$

where I_0 is the saturation current, e is the electron charge, k_B is the Boltzmann constant and I_{ph} is the photocurrent.

In particular, the ideality factor is equal to 1 (ideal diode) if the current is limited by the recombination of minority carriers in the depletion zone (Langevin recombination), and $n_{\mathrm{id}} = 2$ if the recombination involving trapped levels in the spatial region of charge is dominant (Shockley-Read-Hall recombination) [s14,s15].

An expression for the ideality factor of a photodiode can be derived from the diode equation (eq. S5) for $I_{\mathrm{sd}} = 0$:

$$V_{\mathrm{oc}} = n_{\mathrm{id}} \left(\frac{k_{\mathrm{B}} T}{q} \right) \ln\left(\frac{I_{\mathrm{ph}}}{I_0} + 1 \right) \qquad \text{(S6)}$$

If the photocurrent scales linearly with the incident effective power P_{eff}, and $I_{\mathrm{ph}}/I_0 \gg 1$:

$$V_{\mathrm{oc}} = n_{\mathrm{id}} \left(\frac{k_{\mathrm{B}} T}{q} \right) \ln(P_{\mathrm{eff}}) + K(T) \qquad \text{(S7)}$$

$$n_{\mathrm{id}} = \left(\frac{q}{k_{\mathrm{B}} T} \right) \frac{\mathrm{d}V_{\mathrm{oc}}}{\mathrm{d}(\ln(P_{\mathrm{eff}}))} \qquad \text{(S8)}$$

Fitting the experimental values of V_{oc} as a function of P_{eff} to eq. S7 (Fig. S3b and Fig. 2d in the main text) yields a value of $n_{\mathrm{id}} = 1.98$, which indicates that the $FePS_3$/1L-MoS_2 diode photo-response is dominated by SRH recombination assisted by trapped states.

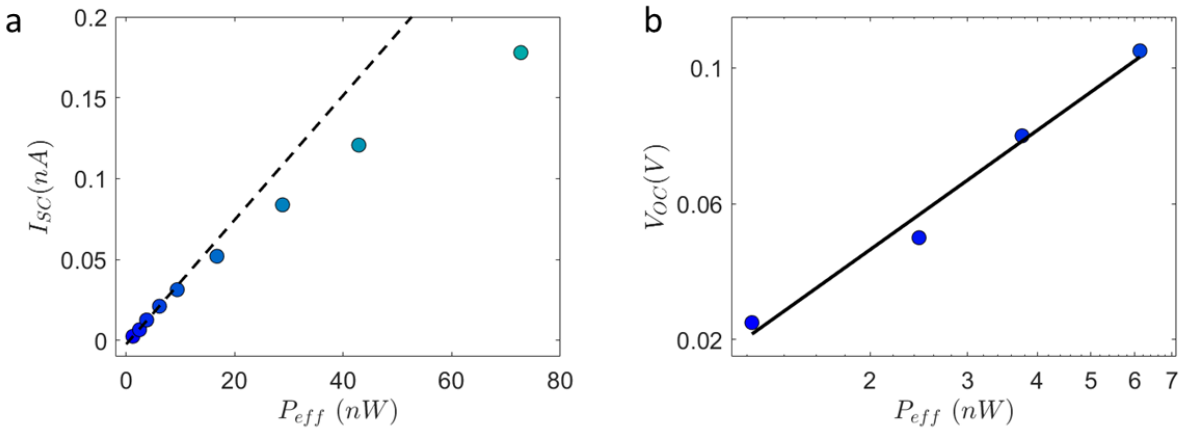

Figure S5. (a) Linear fit to I_{sc} data for the power range where I_{sc} grows linearly with P_{eff} ($I_{sc} \propto P_{eff}$) (device *A*). (b) Linear fit to V_{OC} data the effective power values that satisfy $I_{sc} \propto P_{eff}$. The slope of the fitting curve is $dV_{oc}/d\left(ln\left(P_{eff}\right)\right)$ = 0.051.

S6. Power conversion efficiency for $FePS_3$/1L-MoS_2 (device *A*).

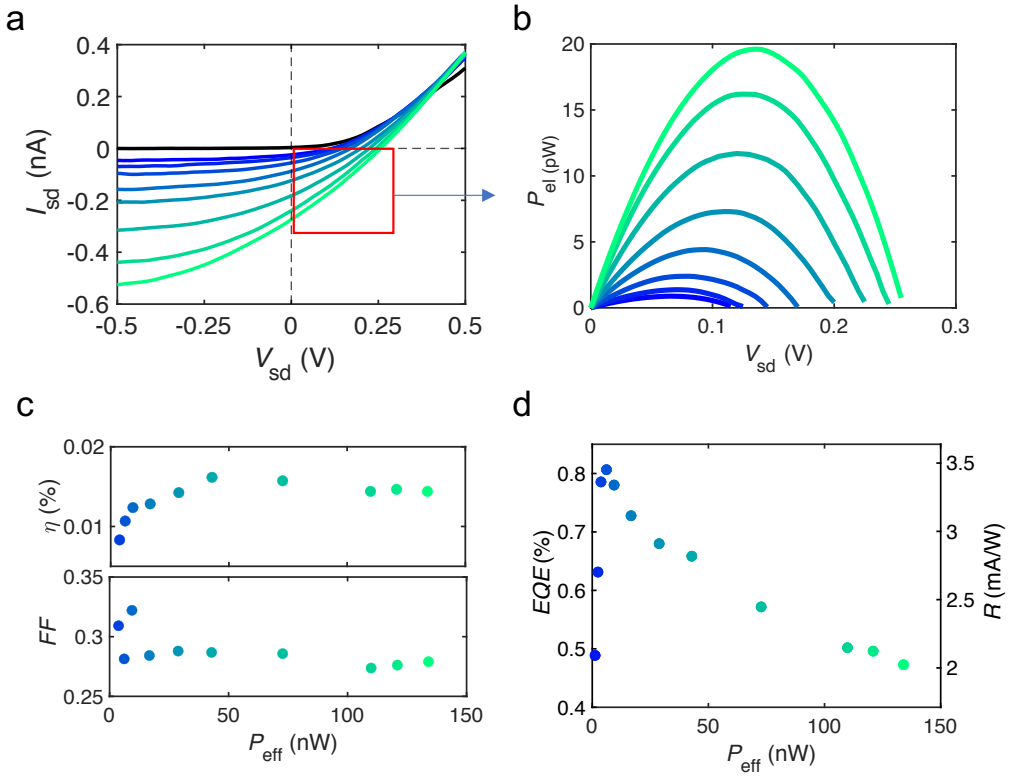

Figure S6. (a) I_{sd}-V_{sd} characteristics of device *A* (same plot as Fig. 2a in the main text). The red square highlights the quadrant in which the device is evaluated for power conversion. (b) Electrical power produced by the photovoltaic cell (device *A*) as a function of the source-drain voltage at several incident, effective, optical powers. The range of effective powers used goes from 1.2 nW (blue) up to 130 nW (green). (c) Power conversion efficiency (top) and fill factor (bottom) as a function of effective power. (d) Corresponding external quantum efficiency and responsivity at $V_{sd} = 0$ upon illumination with 530 nm light.

The fourth quadrant of the $I_{sd} - V_{sd}$ curve in Fig. S6a (Fig. 2a of the main text), which is delimited by $I_{sd} = I_{sc}$ and $V_{sd} = V_{oc}$, defines the region in which the device can be tested as a photovoltaic solar cell. The electrical power delivered by the cell is defined as the product between the applied voltage and the output current: $P_{el} = I_{sd} \cdot V_{sd}$. A maximum value of $P_{el,m} =$ 19.6 pW is obtained at $V_m = 0.14$ V upon illumination at $P_{eff} = 130$ nW. The power conversion efficiency of the cell, η, is defined as the ratio between the maximum electrical power delivered by the cell and the effective illumination power, $\eta = P_{el,m}/P_{eff}$. The fill factor *FF* is defined as the ration between the electrical power delivered by the cell and the ideal maximum given by $P_{el,ideal} = I_{sc} \cdot V_{oc}$.

Table S3. Power conversion efficiency and fill factor for different van der Waals heterostructure devices.

Layer structure		**Device performance**		**Reference**
		***η* (%)**	***FF***	
Containing single-layer TMDs	Black P (11 nm) /1L-MoS_2	0.57	~ 0.5	[s9]
	WSe_2/1L-MoS_2	0.2	~ 0.5	[s15]
	WSe_2/1L-MoS_2	0.4	-	[s16]
	$FePS_3$/1L-MoS_2	**0.015**	**0.3**	**This work**
Containing multi-layer TMDs	p-MoS_2/n-MoS_2	-	0.46	[s12]
	$ReSe_2$/MoS_2	0.072	0.34	[s13]

S7. EQE and responsivity comparison between van der Waals heterostructures

Table S4. External quantum efficiency EQE at V_{sd} = 0 V for different van der Waals heterostructure devices.

Layer structure		EQE (%)	λ (nm)	Reference
Containing single-layer TMDs	BP/1L-MoS_2	0.3	633	[s9]
	WSe_2/1L-MoS_2	1.5	Halogen lamp (~590 nm)	[s15]
	1L-WSe_2/1L-MoS_2	2.4	532	[s16]
	1L-WSe_2/1L-MoS_2	2	495	[s16]
	WSe_2/1L-MoS_2	12	514	[s17]
	$FePS_3$/1L-MoS_2	1.2	532	This work
	$FePS_3$/1L-MoS_2	**2**	**385**	**This work**
Containing multi-layer TMDs	p-MoS_2/n-MoS_2	4.7	660	[s12]
	$FePS_3$/$MoSe_2$	12	522	[s18]

Table S5. Responsivity for different van der Waals heterostructure devices.

Layer structure		Responsivity (mA/W)	λ (nm)	V_{sd} (V)	Reference
Containing single-layer TMDs	BP /1L-MoS_2	418	633	-2	[s9]
	WSe_2/1L-MoS_2	11	~590 nm (halogen)	-1	[s15]
	1L-WSe_2/1L-MoS_2	2-10	532	0	[s16]
	1L-WSe_2/1L-MoS_2	8	495	0	[s16]
	1L-WSe2/1L-MoSe2	~5	514	-1 V	[s21]
	$FePS_3$/1L-MoS_2	~20	532	-1	This work
	$FePS_3$/1L-MoS_2	**40**	**385**	**-1**	**This work**
Containing multi-layer TMDs	Black P/MoS_2	$8.5\cdot10^3$	500	0.7	[s10]
	p-MoS_2/n-MoS_2	14	660	0	[s12]
	$ReSe_2$/MoS_2	$6.75\cdot10^3$	633	1	[s13]
	$FePS_3$/$MoSe_2$	52	522	0	[s18]
	$FePSe_3$/MoS_2	$3.3\cdot10^4$	265	4	[s19]
	$FePS_3$/ReS_2	$\sim1\cdot10^5$	305	-1	[s20]

S8. Optoelectronic characterization for device *B*

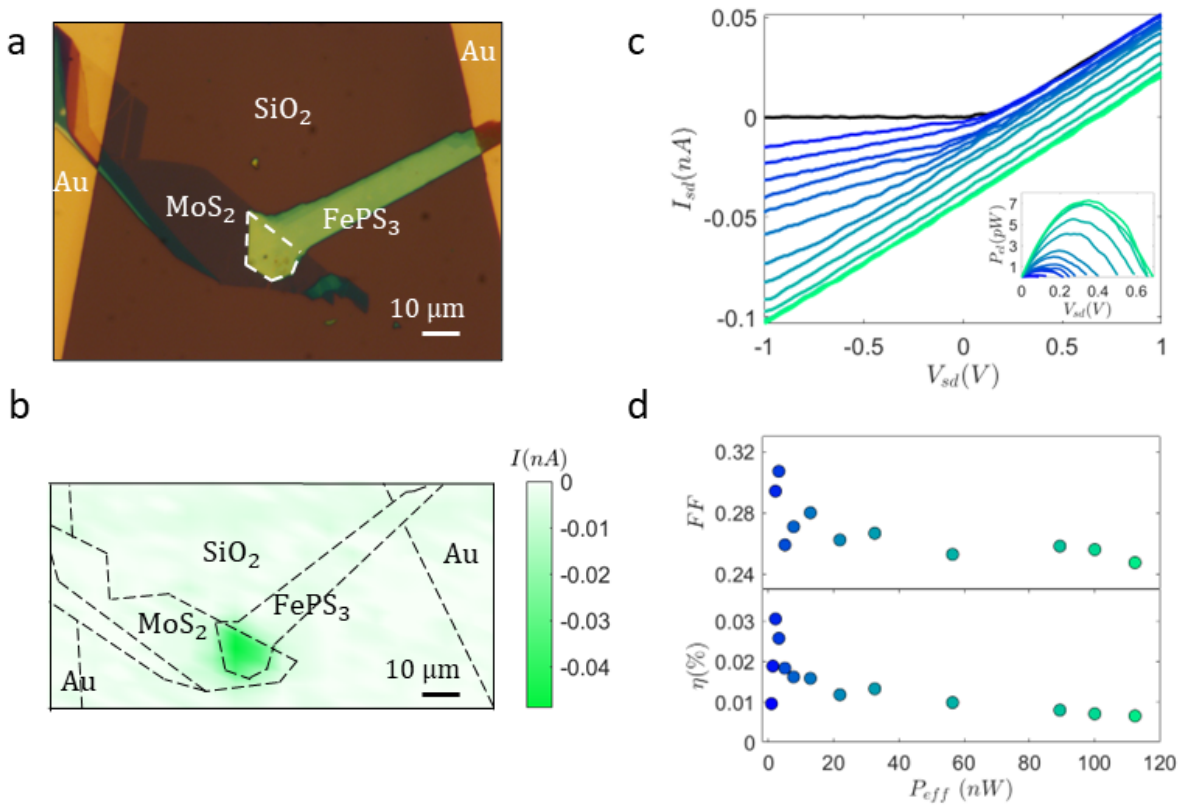

Figure S7. (a) Optical microscopy image of a device *B*. (b) Scanning photocurrent map of device *B*, at $V_{sd} = V_g = 0$V, obtained with an illumination spot of ~ 1 μm diameter and $P_{opt} = 80$ nW. (c) $I_{sd} - V_{sd}$ characteristics at $V_g = 0$ V, upon dark and illumination conditions ($\lambda = 532\ nm$) with optical power up to 120 nW. Inset: Electrical power harvested by the $FePS_3$/1L-MoS_2 p-n junction as a function of the illumination power. (d) Fill factor and power conversion efficiency extracted from panel (c).

S9. Bias voltage dependence of photoluminescence for device *D*

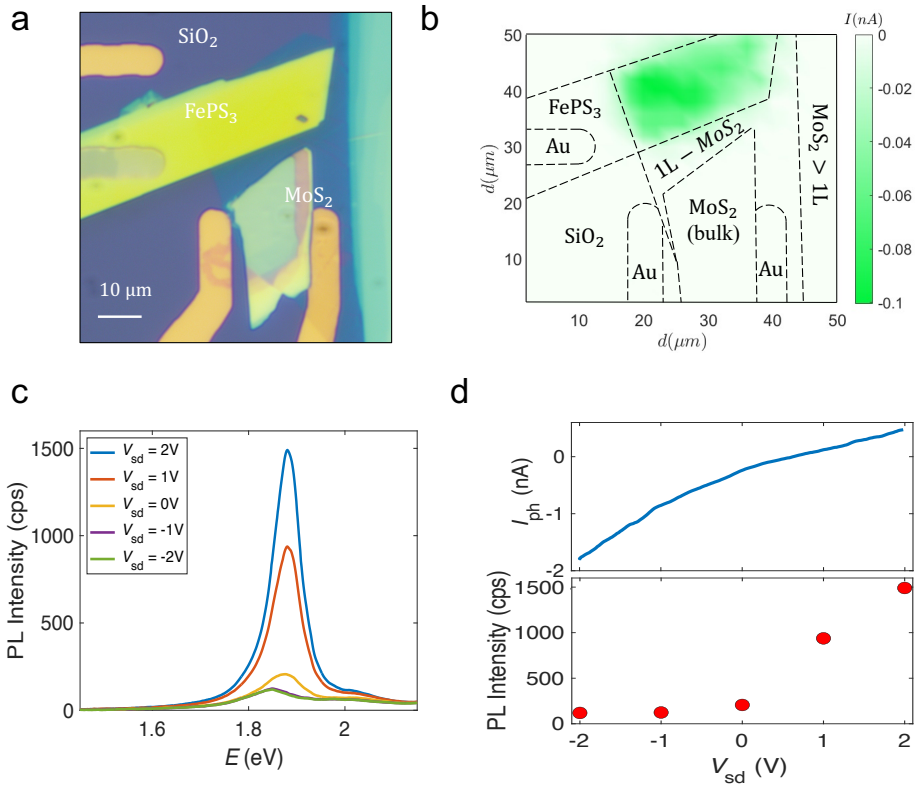

Figure S8. (a). Optical microscopy image of device *D*. (b) Scanning photocurrent map for the same device at zero applied bias voltage. (c) Photoluminescence emission from device *D* as a function of the applied bias voltage for a P_{eff} = 180 μW and λ = 532 nm. (d) Photocurrent $I_{ph} = I_{light} - I_{dark}$ (top) and PL maximum intensity (bottom) as a function of the applied bias voltage.

S10. Photocurrent maps under applied bias

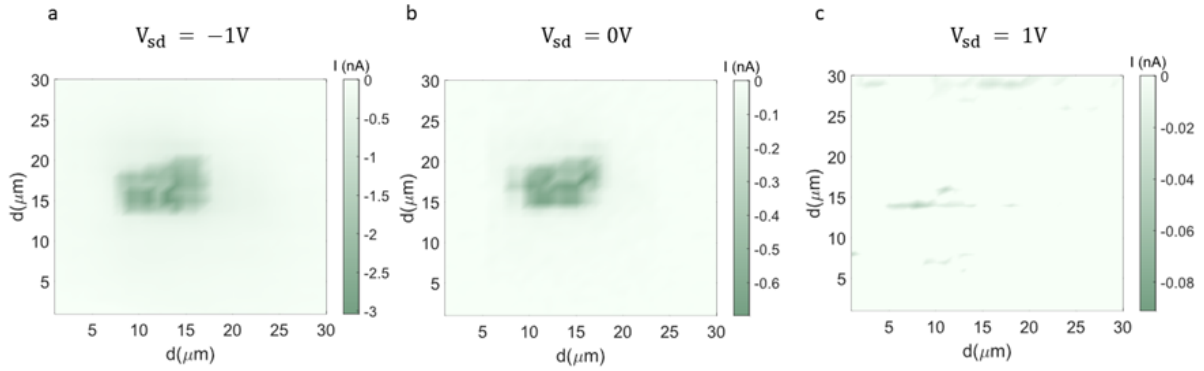

Figure S9. Photocurrent maps for device *C* at different bias voltage V_{sd}. Maps are recorded using a 532 nm laser for excitation with a spot size of ~1 μm diameter and an effective power of P_{opt} = 72 nW.

S11. Gate dependence of dark and bright I_{sd}-V_{sd} characteristics for device *B*

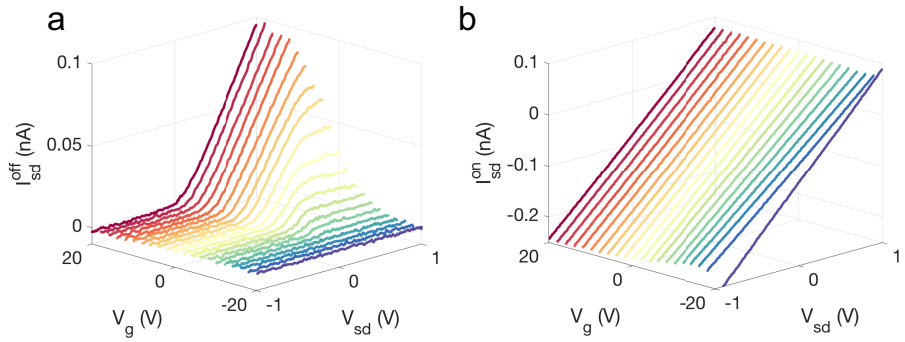

Figure S10. I_{sd} as a function of V_{sd} and V_g in (a) dark and (b) upon illumination with λ = 530 nm and P_{eff} = 95nW.

S12. Raman spectroscopy for device *A*

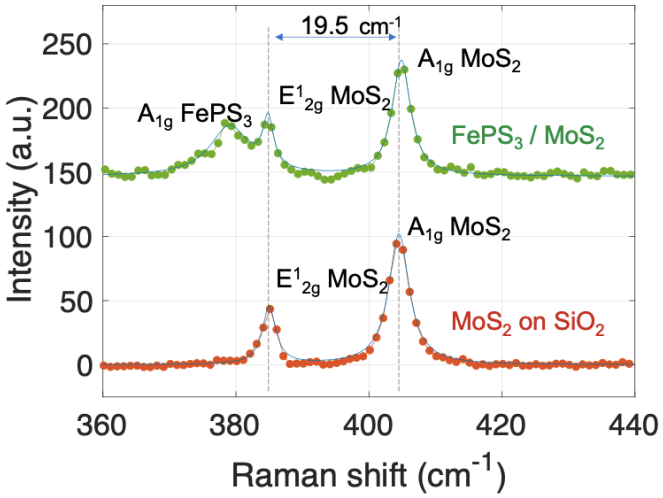

Figure S11. Raman spectra for device *A* at a spot on the 1L-MoS_2 on SiO_2/Si (red curve) and at a spot at the junction with $FePS_3$ (green curve). Spectra were taken using a 532 nm excitation line with 100 μW power.

S13. Spectral weights for trions and neutral excitons in $FePS_3$/1L-MoS_2 devices as a function of applied bias

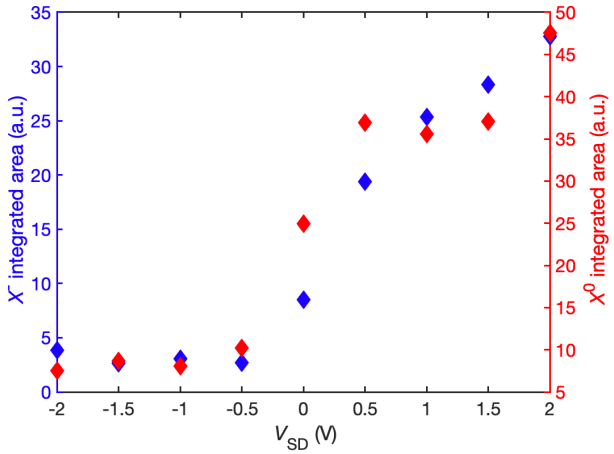

Figure S12. Trion (blue) and neutral exciton (red) spectral weights obtained from a three-Lorentzian fit to the PL spectra shown in Figure 3a of the main manuscript, as a function of the applied bias voltage.

Supplementary References

s1. Ramos, M.; Carrascoso, F.; Frisenda, R.; Gant, P.; Mañas-Valero, S.; Esteras, D. L.; Baldoví J.J.; Coronado E.; Castellanos-Gomez, A.; Calvo, M. R. Ultra-broad spectral photo-response in FePS3 air-stable devices. *npj 2D Materials and Applications* **2021**, *5* (1), 19. https://doi.org/10.1038/s41699-021-00199-z.

s2. Byrnes, S.J. Multilayer optical calculations. *arXiv preprint arXiv:1603.02720* (2016).

s3. Palik E. D. *Handbook of Optical Constants of Solids.* Academic, New York (1991).

s4. Mak, K. F.; He, K.; Lee, C.; Lee, G. H.; Hone, J.; Heinz, T. F.; Shan, J. Tightly Bound Trions in Monolayer MoS2. *Nature Materials* **2013**, *12* (3), 207–211. https://doi.org/10.1038/nmat3505.

s5. Mouri, S.; Miyauchi, Y.; Matsuda, K. Tunable Photoluminescence of Monolayer MoS2 via Chemical Doping. *Nano Letters* **2013**, *13* (12), 5944–5948. https://doi.org/10.1021/nl403036h.

s6. Ramos, M.; Marques-Moros, F.; Esteras, D. L.; Mañas-Valero, S.; Henríquez-Guerra, E.; Gadea, M.; Baldoví, J. J.; Canet-Ferrer, J.; Coronado, E.; Calvo, M. R. Photoluminescence Enhancement by Band Alignment Engineering in MoS2/FePS3 van Der Waals Heterostructures. *ACS Appl. Mater. Interfaces* **2022**, *14* (29), 33482–33490. https://doi.org/10.1021/acsami.2c05464.

s7. Radisavljevic, B.; Radenovic, A.; Brivio, J.; Giacometti, V.; Kis, A. Single-layer MoS2 transistors. *Nature nanotechnology* **2011**, *6*(3), 147-150.

s8. Fuhrer, M. S.; Hone, J. Measurement of mobility in dual-gated MoS2 transistors. *Nature nanotechnology* **2013**, *8*(3), 146-147.

s9. Deng, Y.; Luo, Z.; Conrad, N. J.; Liu, H.; Gong, Y.; Najmaei, S.; Ajayan, P. M.; Lou, J.; Xu, X.; Ye, P. D. Black Phosphorus–Monolayer MoS_2 van Der Waals Heterojunction p–n Diode. *ACS Nano* **2014**, *8* (8), 8292–8299. https://doi.org/10.1021/nn5027388.

s10. Jiang, X.; Zhang, M.; Liu, L.; Shi, X.; Yang, Y.; Zhang, K.; Zhu, H.; Chen, L.; Liu, X.; Sun, Q.; Zhang, D. W. Multifunctional Black Phosphorus/MoS_2 van Der Waals Heterojunction. *Nanophotonics* **2020**, *9* (8), 2487–2493. https://doi.org/10.1515/nanoph-2019-0549.

s11. Molina-Mendoza, A. J.; Giovanelli, E.; Paz, W. S.; Niño, M. A.; Island, J. O.; Evangeli, C.; Aballe, L.; Foerster, M.; Van Der Zant, H. S. J.; Rubio-Bollinger, G.; Agraït, N.; Palacios, J. J.; Pérez, E. M.; Castellanos-Gomez, A. Franckeite as a Naturally Occurring van Der Waals Heterostructure. *Nat Commun* **2017**, *8* (1), 14409. https://doi.org/10.1038/ncomms14409.

s12. Svatek, S. A.; Antolin, E.; Lin, D.-Y.; Frisenda, R.; Reuter, C.; Molina-Mendoza, A. J.; Muñoz, M.; Agraït, N.; Ko, T.-S.; De Lara, D. P.; Castellanos-Gomez, A. Gate Tunable Photovoltaic Effect in MoS $_2$ Vertical p–n Homostructures. *J. Mater. Chem. C* **2017**, *5* (4), 854–861. https://doi.org/10.1039/C6TC04699A.

s13. Wang, X.; Huang, L.; Peng, Y.; Huo, N.; Wu, K.; Xia, C.; Wei, Z.; Tongay, S.; Li, J. Enhanced Rectification, Transport Property and Photocurrent Generation of Multilayer ReSe2/MoS2 p–n Heterojunctions. *Nano Res.* **2016**, *9* (2), 507–516. https://doi.org/10.1007/s12274-015-0932-6.

s14. Shockley, W.; Read, W. T. Statistics of the Recombinations of Holes and Electrons. *Phys. Rev.* **1952**, *87* (5), 835–842. https://doi.org/10.1103/PhysRev.87.835.

s15. Furchi, M. M.; Pospischil, A.; Libisch, F.; Burgdörfer, J.; Mueller, T. Photovoltaic Effect in an Electrically Tunable van Der Waals Heterojunction. *Nano Lett.* **2014**, *14* (8), 4785–4791. https://doi.org/10.1021/nl501962c.

s16. Lee, C.-H.; Lee, G.-H.; van der Zande, A. M.; Chen, W.; Li, Y.; Han, M.; Cui, X.; Arefe, G.; Nuckolls, C.; Heinz, T. F.; Guo, J.; Hone, J.; Kim, P. Atomically Thin p–n Junctions with van Der Waals Heterointerfaces. *Nature Nanotech* **2014**, *9* (9), 676–681. https://doi.org/10.1038/nnano.2014.150.

s17. Cheng, R.; Li, D.; Zhou, H.; Wang, C.; Yin, A.; Jiang, S.; Liu, Y.; Chen, Y.; Huang, Y.; Duan, X. Electroluminescence and Photocurrent Generation from Atomically Sharp WSe $_2$ /MoS $_2$ Heterojunction *p–n* Diodes. *Nano Lett.* **2014**, *14* (10), 5590–5597. https://doi.org/10.1021/nl502075n.

s18. Duan, J.; Chava, P.; Ghorbani-Asl, M.; Lu, Y.; Erb, D.; Hu, L.; Echresh, A.; Rebohle, L.; Erbe, A.; Krasheninnikov, A. V.; Helm, M.; Zeng, Y.-J.; Zhou, S.; Prucnal, S. Self-Driven Broadband Photodetectors Based on MoSe $_2$ /FePS $_3$ van Der Waals n–p Type-II Heterostructures. *ACS Appl. Mater. Interfaces* **2022**, *14* (9), 11927–11936. https://doi.org/10.1021/acsami.1c24308.

s19. Long, M.; Shen, Z.; Wang, R.; Dong, Q.; Liu, Z.; Hu, X.; Hou, J.; Lu, Y.; Wang, F.; Zhao, D.; Ding, F.; Tu, Y.; Han, T.; Li, F.; Zhang, Z.; Hou, X.; Wang, S.; Shan, L. Ultrasensitive Solar-Blind Ultraviolet Photodetector Based on FePSe $_3$ /MoS $_2$ Heterostructure Response to 10.6 Mm. *Adv Funct Materials* **2022**, *32* (34), 2204230. https://doi.org/10.1002/adfm.202204230.

s20. Gao, H.; Du, C.; Sun, J.; Zhang, J.; Leng, J.; Li, J.; Wang, W.; Li, K. Enhanced Optoelectronic Performances of FePS3/ReS2 Van Der Waals Heterostructures with Type-II Band Alignment. *Materials Today Communications* **2023**, *35*, 105959. https://doi.org/10.1016/j.mtcomm.2023.105959.

s21. Gong, Y.; Lei, S.; Ye, G.; Li, B.; He, Y.; Keyshar, K.; Zhang, X.; Wang, Q.; Lou, J.; Liu, Z.; Vajtai, R.; Zhou, W.; Ajayan, P. M. Two-Step Growth of Two-Dimensional WSe2/MoSe2 Heterostructures. *Nano Lett.* **2015**, *15* (9), 6135–6141. https://doi.org/10.1021/acs.nanolett.5b02423.